Electronic Supplementary Information

Porous bismuth antimony telluride alloys with excellent thermoelectric and mechanical properties

Peng Zhao, Fengrong Yu, Binhao Wang, Haidong Zhao, Chen Chen, Dan Wang, Pan Ying, Yingju Wu, Penghui Li, Bin Zhang, Bing Liu, Zhisheng Zhao, Wentao Hu, Dongli Yu, Julong He, Zhongyuan Liu, Bo Xu*****, and Yongjun Tian

Center for High Pressure Science, State Key Laboratory of Metastable Materials Science and Technology, Yanshan University, Qinhuangdao, Hebei 066004, China

*****_Corresponding author. E-mail address: bxu@ysu.edu.cn_

Orientation factor F

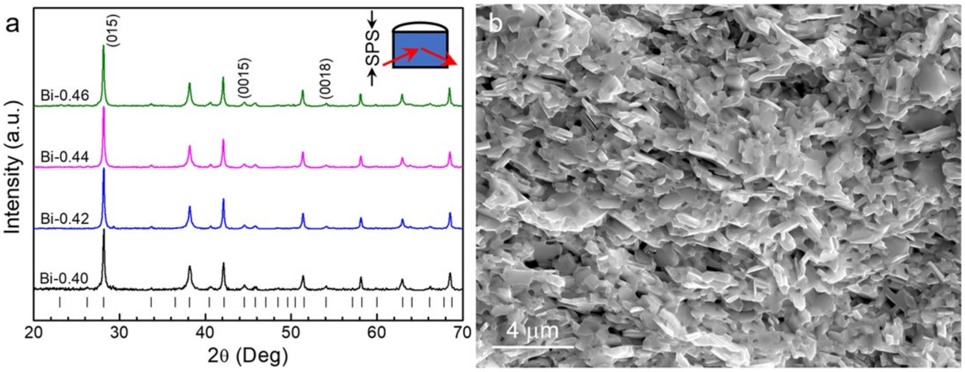

Figure S1. Structure characterization of porous $Bi_xSb_{2-x}Te_3$ samples from the surfaces parallel to SPS compressing. a) XRD patterns. b) SEM image of the fracture surface parallel to the compressing direction of a porous $Bi_{0.42}Sb_{1.58}Te_3$ sample.

Figure S1a displays the XRD patterns of porous BiSbTe bulks taken from the surfaces parallel to SPS compressing, showing much weaker (00*l*) peaks than those from the perpendicular surfaces and suggesting a preferential orientation of grains in the bulks. We calculated the orientation factor, *F*, of porous BiSbTe bulks based on the XRD patterns from the surfaces perpendicular to surface SPS compressing (with stronger (00*l*) peaks) using the Lotgering method[1]

$$F = \frac{P - P_0}{1 - P_0}$$

Where $P_0 = \sum I_0(00l) / \sum I_0(hkl)$ and $P = \sum I(00l) / \sum I(hkl)$ are ratios of the integrated intensity of all (00*l*) planes to that of all (*hkl*) for preferentially and randomly oriented samples, respectively. The calculated values are listed in Table S1, indicating a minor degree of texture in the porous samples.

Table S1. Orientation factor, *F*, of the porous $Bi_xSb_{2-x}Te_3$ (P-Bi-*x*) samples and the dense control sample of $Bi_{0.42}Sb_{1.58}Te_3$ (CS-Bi-0.42)

Sample	P-Bi-0.40	P-Bi-0.42	P-Bi-0.44	P-Bi-0.46	CS-Bi-0.42
F	0.044	0.036	0.032	0.027	0.097

Figure S2 displays the structure of a dense control sample of $Bi_{0.42}Sb_{1.58}Te_3$, showing an obvious preferential orientation and much larger plate-like grains. The orientation factor is listed in Table S1.

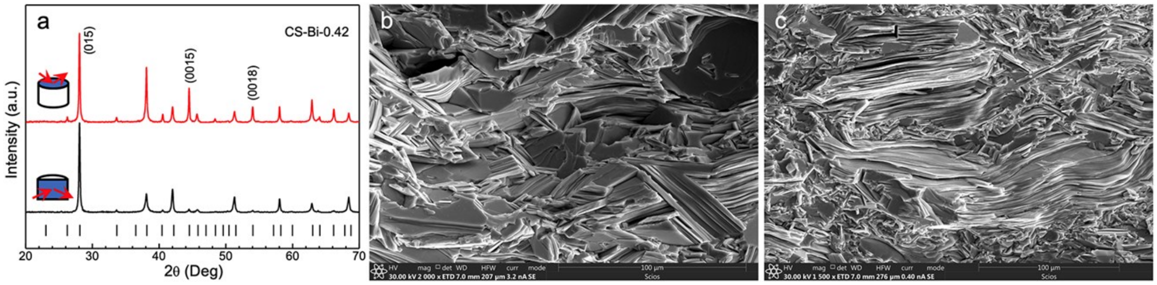

Figure S2. The structure of CS-Bi-0.42 without ball milling (HPS+SPS). a) XRD patterns from the surfaces perpendicular (red) and parallel (black) to the uniaxial compressing direction of SPS. b) The fracture surface perpendicular to SPS compressing. c) The fracture surface parallel to SPS compressing.

The formation of porous structure

We ascribed the formation of porous structure to the fine-structured BM powders, which are agglomerated by a large number of randomly oriented nanograins (10–20 nm in size), and the mild SPS conditions (18 MPa and 663 K for 5 min). To corroborate this argument, we prepared different samples with various starting materials, BM duration, or SPS conditions, as listed in Table S2.

Table S2. Sample information. The porosity was estimated from the density. Note Sample Bi-0.42-R was prepared with the same conditions as p-Bi-0.42 (i.e., a repeated sample).

Sample name	Starting material	BM duration	SPS parameters	Porosity
ES	Bi, Sb, and Te (0.5:1.5:3)	72 hours	18 MPa, 663 K, 5 min	15.1%
ZM	$Bi_{0.5}Sb_{1.5}Te_3$ zone melting ingot	72 hours	18 MPa, 663 K, 5 min	15.3%
Bi-0.42-R	HPS $Bi_{0.42}Te_{1.58}Te_3$	72 hours	18 MPa, 663 K, 5 min	14.2%
BM-3h	HPS $Bi_{0.42}Te_{1.58}Te_3$	3 hours	18 MPa, 663 K, 5 min	5.1%
SPS-50MPa	HPS $Bi_{0.42}Te_{1.58}Te_3$	72 hours	50 MPa, 663 K, 5 min	6.3%
CS-Bi-0.42	HPS $Bi_{0.42}Te_{1.58}Te_3$	manual grinding	18 MPa, 663 K, 5 min	4.0%

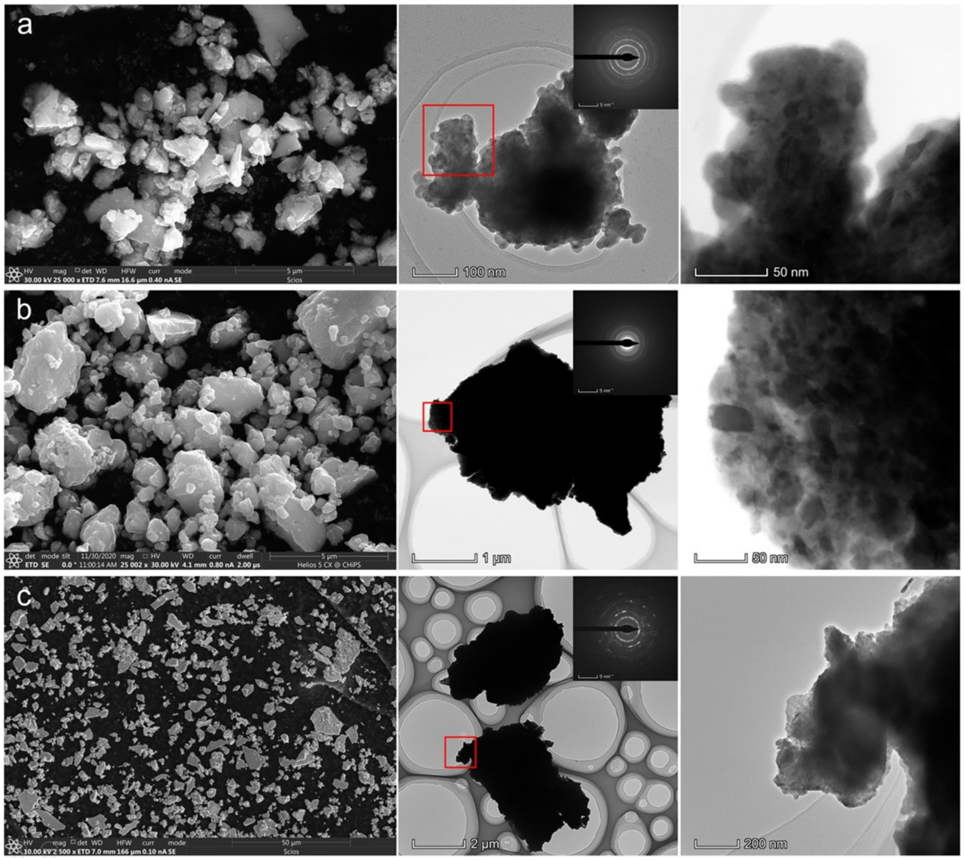

Figure S3. Structural characterization of different BM powders. a) 72h BM powders from elementary substance (ES). b) 72h BM powders from ZM ingot (ZM). c) 3h BM powders from HPS product (BM-3h). From left to right: SEM image, TEM image, and HRTEM image (form the selected area in TEM). The inset shows the SAED pattern of the powder, indicating a polycrystallinity.

Figure S3 show the morphology of BM powders for ES, ZM, and BM-3h samples. BM powders from elementary and zone melting starting materials exhibit morphology similar to that of BM powders from HPS starting material (Figure 1) after 72 hours of ball milling: Numerous BiSbTe nanograins (10–20 nm in size) are agglomerated into powders with size ranging from submicron to several microns. However, the 3h BM powders from HPS starting material show a much broader size distribution: In addition to the nanograin agglomerations, a plurality of BiSbTe flakes with size up to 10 microns are clearly observed, indicating an insufficient BM process.

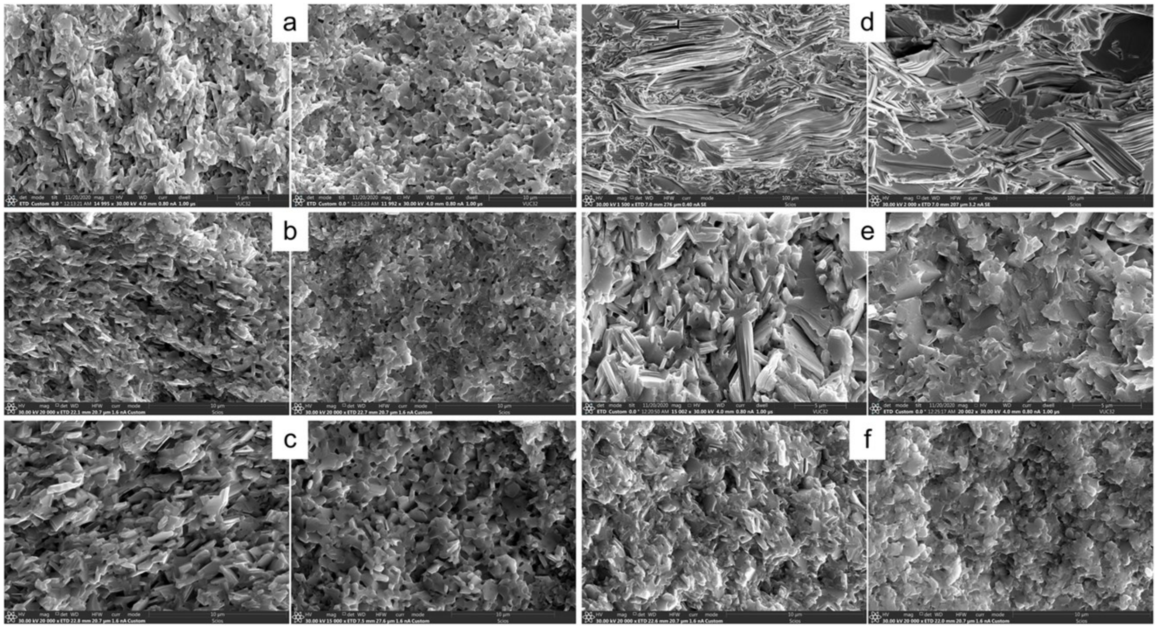

Figure S4. SEM images of fractured surfaces parallel (left) and perpendicular (right) to SPS compressing. a) Bi-0.42-R. b) ES. c) ZM. d) CS-Bi-0.42. e) BM-3h. f) SPS-50MPa.

With five different powders (*i.e.*, 72h-BM ES, ZM, and HPS, 3h-BM HPS, and manual-ground HPS), we prepared 6 samples with SPS (Table S2). Figure S4 shows SEM images of these samples taken from fractured surfaces parallel and perpendicular to SPS compressing. ES, ZM, and Bi-0.42-R samples (Figure S4a–c) exhibit porous microstructures similar to that of p-Bi-0.42 (Figure 3 and Figure S1b). In these samples, micron-sized quasi-equiaxed grains are observed with evenly distributed pores and similar porosity (*ca*. 15%), suggesting the specific starting material before the ball milling process does not play a decisive role in the formation of the porous structure. In contrast, CS-Bi-0.42 and BM-3h (Figure S4d–e), with SPS conditions the same as those for ES, ZM, and Bi-0.42-R, show distinct microstructures and are much denser (4–5% in porosity). The manual ground powders and 3h BM powders are featured with BiSbTe flakes, which are easier to condense under pressure. Therefore, the structure and morphology of powders do affect the microstructure of the final SPS products. Note the distinction between CS-Bi-0.42 and BM-3h can be accounted for by the much smaller BiSbTe flakes as well as the presence of nanograin agglomerations in 3h BM powders. Comparison of Bi-0.42-R and SPS-50MP samples (both produced from the 72h-BM HPS powders) reveals similar grain size and shape in the bulk. However, the grains in SPS-50MP are more tightly bound with much fewer pores left, obviously due to the higher SPS pressure.

These samples prepared with different conditions verify our argument on the formation of porous structure. Both the fine-structured BM powders (i.e., agglomeration of nanograins into powder) and the mild SPS conditions are key to the formation of porous structure.

Mechanical properties of samples with distinct microstructure

The mechanical properties (Vickers hardness H_V, bending strength σ_b, and compressive strength σ_c) of the samples listed in Table S2 were measured and shown in Figure S5. All the porous samples show similar values for H_V, σ_b, and σ_c, which is understandable since these samples possess similar microstructure (grain size and shape, porosity). For the dense samples, SPS-50MPa shows the best mechanical properties, and CS-Bi-0.42 the worst. This is consistent with the variation tendency of grain size in the dense samples, *i.e.*, the smaller the grain size, the better the mechanical properties. The Hall–Petch effect that is well-known for metals and ceramics seems also works here.

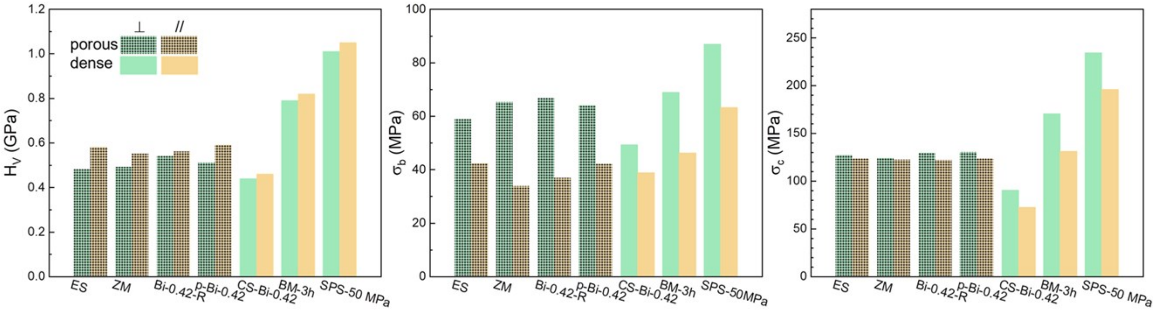

Figure S5. Mechanical properties of different samples. a) Vickers hardness. b) Bending strength. c) Compressive strength. The force loading direction (⊥ or //) are defined by reference to the direction of SPS compression.

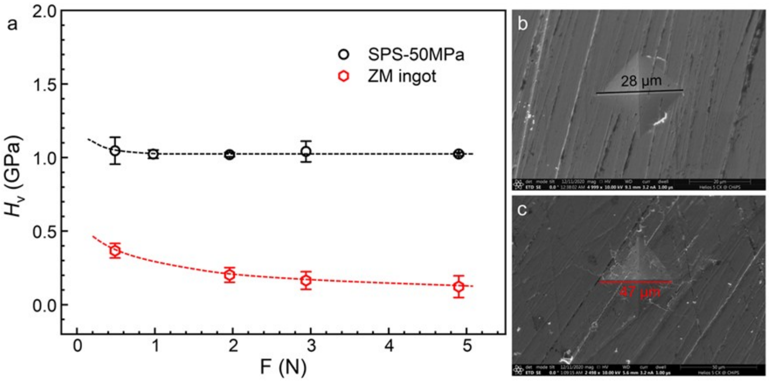

Figure S6. a) Vickers hardness as a function of applied load for SPS-50 MPa sample and a ZM ingot. b) The indentation on SPS-50MPa under a load of 0.49 N. c) The indentation on ZM ingot under a load of 0.49 N. The dash lines are guide to the eyes.

Another evidence of grain refinement strengthening is provided by the direct comparison of Vickers hardness measurements on SPS-50MPa and a ZM ingot. In general, the hardness of a material should be determined from the asymptotic-hardness region where hardness value is invariable with increasing load. As shown in Figure S6, the hardness of SPS-50MPa is maintained at a value slightly higher than 1 GPa, which is the highest hardness value of BiSbTe alloys (under a large load) to the best of our knowledge; in contrast, the hardness of ZM ingot decreases from

0.4 GPa (under a load of 0.49 N) to less than 0.2 GPa (under a load of 4.9 N). The SEM observation of the indentation reveals more significant damage in the ZM ingot.

Therefore, the enhanced mechanical properties of our porous samples can be attributed to the joint effect of grain refinement, tightly-bound quasi-equiaxed grains (both for enhancing), and the introduction of pores (for weakening).

Elemental distribution in the porous sample

The elemental distribution in P-Bi-0.42 bulk was checked with EDS at different length-scales. All elements are evenly distributed in the porous sample with no obvious segregation.

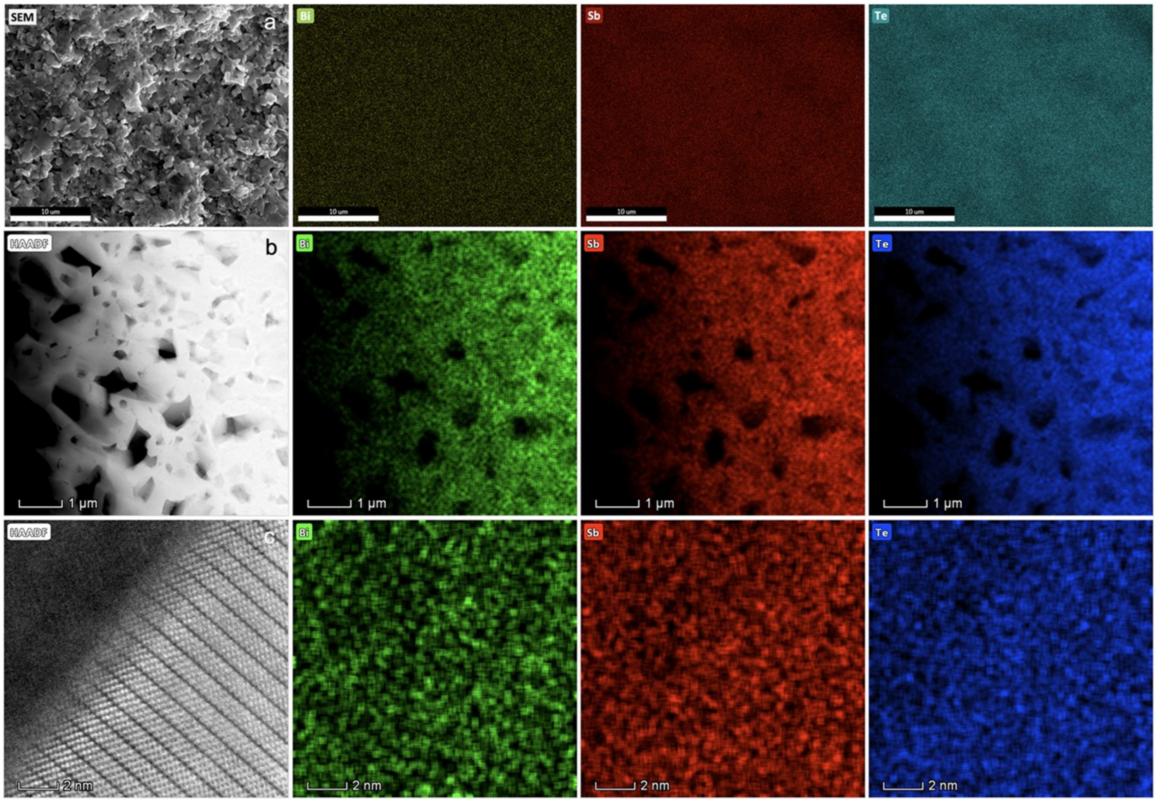

Figure S7. EDS elemental mapping of P-Bi-0.42 bulk. a) SEM image of the fractured surface perpendicular to SPS compressing and the corresponding elemental mapping of Bi, Sb, and Te. b) and c) HAADF-STEM images under different magnification and the corresponding elemental mapping of Bi, Sb, and Te.

Anisotropy in thermoelectric properties of porous BiSbTe samples

Temperature dependent thermoelectric properties of P-Bi-*x* samples were measured in the direction parallel to SPS compressing (Figure S8). Both electrical transport and thermal conductivity show anisotropy consistent with that revealed in the microstructure. Nonetheless, all the porous samples show more or less the same (maximal and average) *ZT* values in both perpendicular and parallel directions.

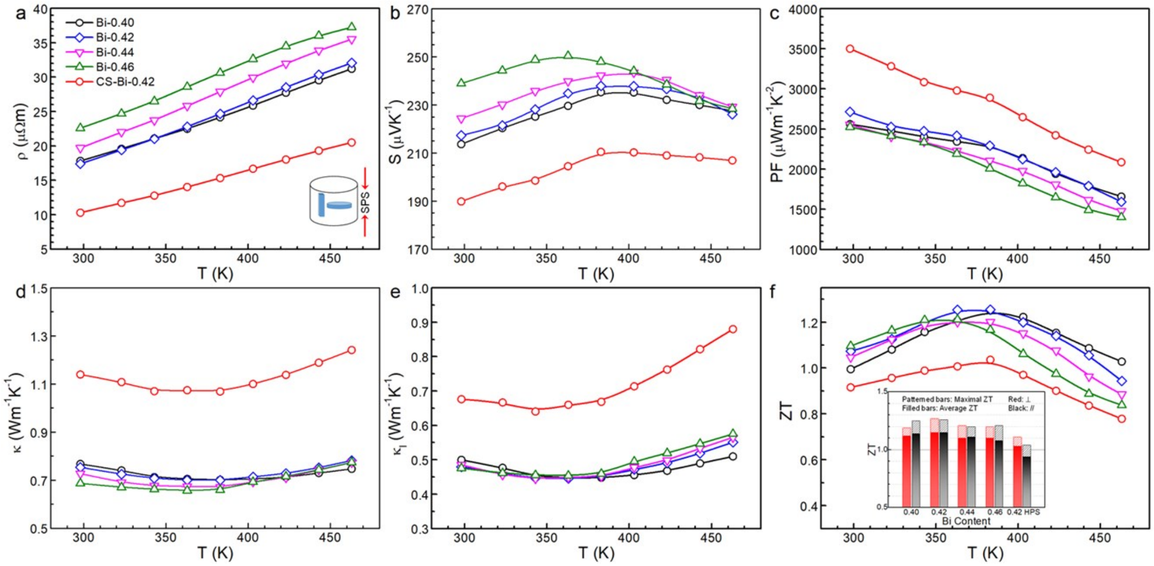

Figure S8. Temperature dependent thermoelectric properties of P-Bi-*x* samples measured in the direction parallel to SPS compressing. The dense CS-Bi-0.42 sample (without BM) was included for comparison. a) Electrical resistivity. b) Seebeck coefficient. c) Power factor. d) Total thermal conductivity. e) Lattice thermal conductivity. f) Dimensionless figure of merit, where the inset shows maximal *ZT* and average *ZT* (298–463 K) of different samples.

Thermal stability of P-Bi-0.42 bulk

The thermal stability of thermoelectric properties was investigated with repeated measurements for P-Bi-0.42 sample, indicating an excellent stability. In addition, the microstructures of the sample after all the tests were checked with SEM, further confirming the structure stability.

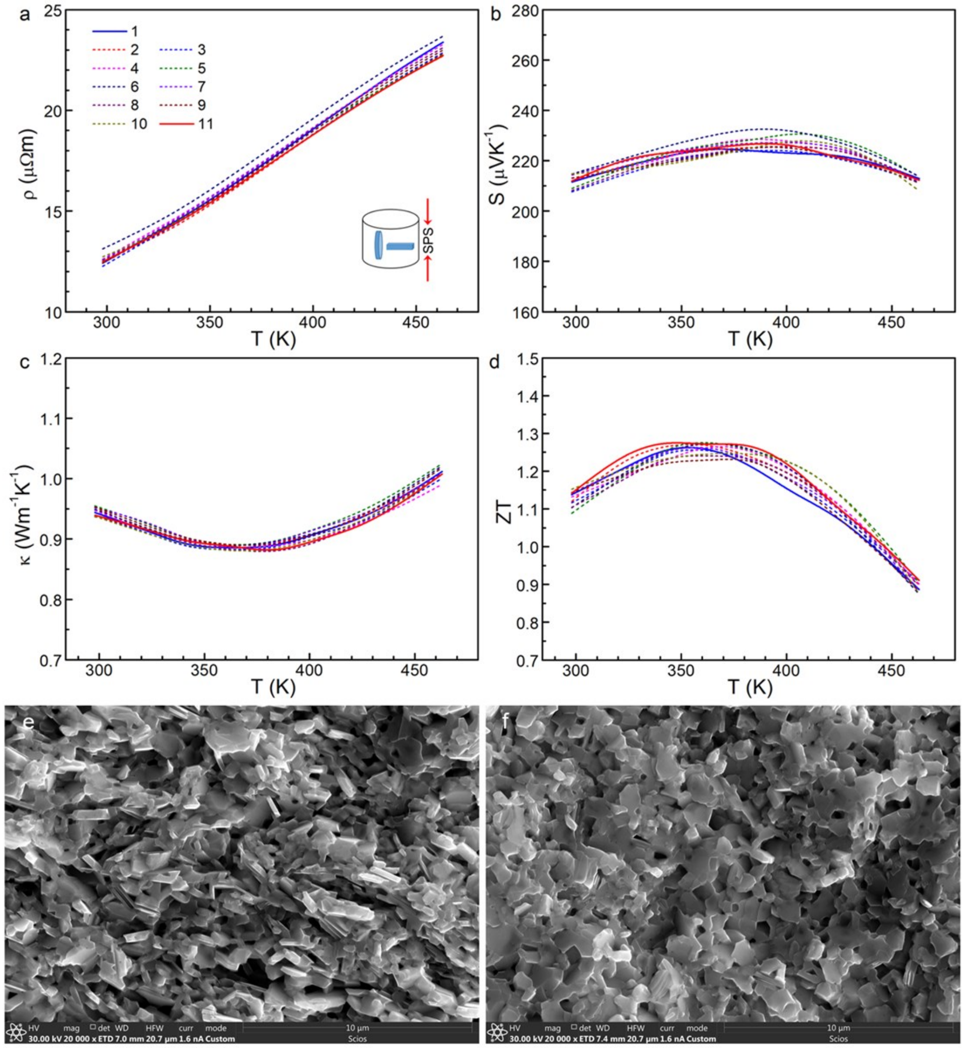

Figure S9. Thermal stability of P-Bi-0.42. Ten more thermoelectric properties measurements were performed after the first one. a) Electrical resistivity. b) Seebeck coefficient. c) Thermal conductivity. d) *ZT*. e) The fractured surface (parallel to SPS compressing) of the rectangular bar after 11 times electrical transport measurements. f) The fractured surface (perpendicular to SPS compressing) of the rectangular bar after 11 times electrical transport measurements. The measurement direction was perpendicular to SPS compressing.

Lattice thermal conductivity quantification

In the Debye-Callaway theory, the lattice thermal conductivity can be expressed as:[2]

$$\kappa_l = \frac{k_\mathrm{B}}{2\pi^2 v}\left(\frac{k_\mathrm{B}T}{\hbar}\right)^3 \int_0^{\theta_\mathrm{D}/T} \tau(x)\frac{e^x x^4}{\left(e^x-1\right)^2}\mathrm{d}x$$

where $x = \hbar\omega/k_\mathrm{B}T$ is the reduced phonon frequency, v the in-plane average sound speed, and $\tau(x)$ the relaxation time. In BiSbTe alloys, the phonon scattering mechanisms include the phonon-phonon Umklapp scattering (U), point defect scattering (PD), grain boundary scattering (B), and dislocation scattering (D), and the total phonon relaxation time can be determined by the Matthiassen's rule:[3]

$$\tau(x)^{-1} = \tau_\mathrm{U}^{-1} + \tau_\mathrm{PD}^{-1} + \tau_\mathrm{B}^{-1} + \tau_\mathrm{D}^{-1}$$

$$\tau_\mathrm{U}^{-1} = Ax^2T^3$$

where A is the pre-factor of Umklapp scattering time that is obtained by fitting the in-plane transport parameters of the ZM sample.[4]

$$\tau_\mathrm{PD}^{-1} = \frac{k_\mathrm{B}^4 V_\mathrm{PUC}}{4\pi\hbar^4 v^3}\Gamma x^4 T^4, \text{ with } \Gamma = \sum_i f_i\left(\frac{M_i-\overline{M}}{\overline{M}}\right)^2$$

where V_PUC is the volume of the primitive unit cell, Γ is the point defect scattering parameter that is determined by the mass difference of compositional elements.[5,6]

$$\tau_\mathrm{B}^{-1} = \frac{v}{d}$$

where d is the grain size.

$$\tau_\mathrm{DS}^{-1} = N_\mathrm{D}\frac{\overline{V}^{4/3}}{v^2}\left(\frac{xk_\mathrm{B}T}{\hbar}\right)^3 + 0.6B_\mathrm{D}^2 N_\mathrm{D}\left(\gamma+\gamma_0\right)^2\frac{xk_\mathrm{B}T}{\hbar}\left\{\frac{1}{2}+\frac{1}{24}\left(\frac{1-2r}{1-r}\right)^2\left[1+\sqrt{2}\left(\frac{v_\mathrm{L}}{v_\mathrm{T}}\right)^2\right]^2\right\}$$

$$\text{with } \gamma_0 = \frac{V_\mathrm{ST}C_0K}{k_\mathrm{B}T_\mathrm{a}}\left(\gamma\alpha^2-\alpha\beta\right),\ \alpha = \frac{V_\mathrm{BT}-V_\mathrm{ST}}{V_\mathrm{ST}},\ \beta = \frac{M_\mathrm{ST}-M_\mathrm{BT}}{2M_\mathrm{ST}},$$

where N_D, B_D, γ, C_0, K, T_a, and r are the dislocation density, Burger's vector, Grüneisen parameter, concentration of $\mathrm{Bi_2Te_3}$ in BiSbTe alloy, bulk modulus of $\mathrm{Bi_2Te_3}$, sintering temperature, and Poisson's ratio, respectively.

κ_l for the porous sample is then estimated as

$$\kappa_{l,\,\text{porous}} \approx \kappa_l \frac{2-2\phi}{2+\phi}$$

Table S3 lists all the calculation parameters used in the quantification.

Table S3. Parameters in Debye-Callaway model of the lattice thermal conductivity for Bi_2Te_3-based materials.

parameter	value	source
v, in-plane average speed of sound	2147 ms^{-1}	Ref. 7
θ_D, Debye temperature	94 K	Ref. 8
A, pre-factor of Umklapp scattering time	150000 $K^{-3}s^{-1}$	fitting
V_{PUC}, volume of the primitive unit cell	$5\bar{V}$	
$\bar{V}$, average volume per atom	3.13×10^{-29} m^{-3}	Ref. 8
d, grain size	1 μm	experiment
N_D, dislocation density	1.6×10^{-10} cm^{-2}	experiment
B_D, burger's vector	2 nm	Ref. 3
γ, Grüneisen parameter	2.3	Ref. 8
v_L, longitudinal sound velocity	2884 ms^{-1}	Ref. 7
v_T, transverse sound velocity	1780 ms^{-1}	Ref. 7
V_{BT}, atomic volume of Bi_2Te_3	3.4×10^{-29} m^{-3}	Ref. 8
V_{ST}, atomic volume of Sb_2Te_3	3.13×10^{-29} m^{-3}	Ref. 8
M_{BT}, atomic mass of Bi_2Te_3	2.66×10^{-25} Kg	Ref. 8
M_{ST}, atomic mass of Sb_2Te_3	2.07×10^{-25} Kg	Ref. 8
C_0, concentration of Bi_2Te_3 in $Bi_{0.42}Sb_{1.58}Te_3$	0.21	calculation
K, bulk modulus of Bi_2Te_3	44.8 GPa	Ref. 8
T_a, sintering temperature	663 K	experiment
r, Poisson's ratio	0.24	Ref. 8
ϕ, porosity	0.144	experiment

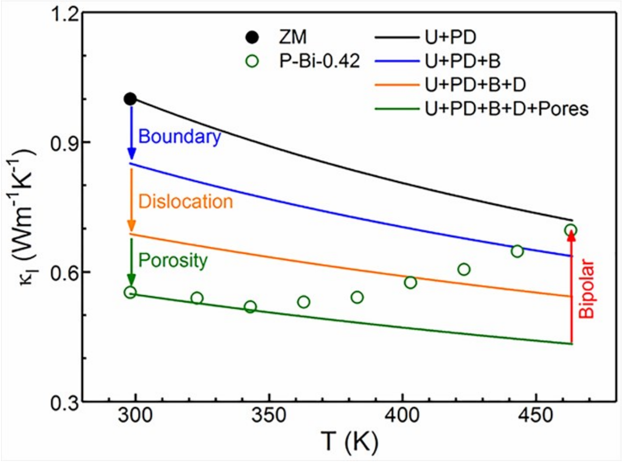

Figure S10. Quantification of lattice thermal conductivity. Green empty symbols shows κ_l of P-Bi-0.42 in the perpendicular direction, while the black symbol κ_l of a ZM sample.[4] The experimental results were accounted for considering porosity and reasonable contributions from Umklapp (U), point defect (PD), boundary (B), and dislocation (D) scattering.

References

1. F. K. Lotgering, *J. Inorg. Nucl. Chem.*, 1959, **9**, 113-123.
2. T. M. Tritt, *Thermal Conductivity: Theory, Properties, and Applications*, Kluwer Academic/Plenum Publishers, New York, 2004.
3. Y. Pan, U. Aydemir, J. A. Grovogui, I. T. Witting, R. Hanus, Y. Xu, J. Wu, C.-F. Wu, F.-H. Sun, H.-L. Zhuang, J.-F. Dong, J.-F. Li, V. P. Dravid and G. J. Snyder, *Adv. Mater.*, 2018, **30**, 1802016.
4. Y. Zheng, Q. Zhang, X. Su, H. Xie, S. Shu, T. Chen, G. Tan, Y. Yan, X. Tang, C. Uher and G. J. Snyder, *Adv Energy Mater*, 2015, **5**, 1401391.
5. H. J. Goldsmid, *J. Appl. Phys.*, 1961, **32**, 2198-2202.
6. H. J. Goldsmid, in *Introduction to Thermoelectricity*, ed. H. J. Goldsmid, Springer Berlin Heidelberg, Berlin, Heidelberg, 2010, ch. 5, pp. 63-78.
7. F. Yang, T. Ikeda, G. J. Snyder and C. Dames, *J. Appl. Phys.*, 2010, **108**, 034310.
8. S. I. Kim, K. H. Lee, H. A. Mun, H. S. Kim, S. W. Hwang, J. W. Roh, D. J. Yang, W. H. Shin, X. S. Li, Y. H. Lee, G. J. Snyder and S. W. Kim, *Science*, 2015, **348**, 109-114.